DOI: 10.1002/chem.200800336

Laves Phases, γ-Brass, and 2×2×2 Superstructures: A New Class of Quasicrystal Approximants and the Suggestion of a New Quasicrystal

Robert F. Berger, Stephen Lee,* Jeffreys Johnson, Ben Nebgen, and Adrian Chi-Yau So[a]

Abstract: Of the most common cubic intermetallic structure types, several ($MgCu_2$, Cu_5Zn_8, Ti_2Ni, and α-Mn) have superstructures with unusual symmetry properties. These superstructures (Be_5Au, $Li_{21}Si_5$, $Sm_{11}Cd_{45}$, and $Mg_{44}Ir_7$) have the unusual property of pairs of perpendicular pseudo fivefold axes, most apparent in their X-ray diffraction patterns. The current work shows that an 8D to 3D projection method cleanly describes most (and in one case, all) of the atomic positions in the four superstructures mentioned above. This type of projection, which maps the E_8 lattice (a mathematically simple 8D crystal) into 3D space, combines the desired higher dimensional point group's perpendicular fivefold rotations with 3D translational symmetry—exactly what we see in the experimental crystal structures. The projection method successfully accounts for all heavy atom positions in the four superstructures, and at least 60–70 % of the light atom positions. The results suggest that all of these structures, previously known to be connected only by qualitative similarities in their atomic "clusters", are approximants of a single, as-yet unknown, class of quasicrystal.

Keywords: higher dimension • intermetallic phases • quasicrystals • solid-state structures • X-ray diffraction

Introduction

To most physical scientists, the world of intermetallic phases is dominated by simple variants of a few familiar structures: face-centered cubic (fcc), hexagonal closest-packed (hcp), and body-centered cubic (bcc). Indeed, these structures can take our understanding a long way, as they account for most metallic elemental structures, as well as many atomically ordered intermetallic compounds and atomically disordered alloys. However, there are also extensive classes of much more complex intermetallic compounds. A deeper understanding of these more complicated phases is necessary if physical scientists are to become fully conversant with metallic structures, and, as metals make up more than two thirds of the periodic table, if we are to appreciate the intricacies of some half of all thermodynamically stable binary compounds.

In this paper, we concentrate on one important branch of these more complicated structures: cubic crystal compounds of purely metallic elements. Pearson's Handbook of Crystallographic Data for Intermetallic Phases[1] shows us that (limiting ourselves to structure types whose compounds often consist entirely of elements in the first twelve columns of the periodic table) the most common complex cubic structure types are quite varied. The $MgCu_2$[2] structure type is found in 807 compounds. In descending order of frequency are then the Cr_3Si[3] (260 compounds), Th_6Mn_{23}[4] (204 compounds), $NaZn_{13}$[5] (91 compounds), Be_5Au[6] (75 compounds), α-Mn[7] (73 compounds), Ti_2Ni[8] (62 compounds), β-Mn[9] (41 compounds), Cu_5Zn_8[10] (39 compounds), $Sm_{11}Cd_{45}$[11] (19 compounds), and YCd_6[12] (19 compounds) structures.

This paper focuses on six of the above eleven structure types: the $MgCu_2$ (the cubic Laves phase), Be_5Au, α-Mn (the χ-phase), Ti_2Ni, Cu_5Zn_8 (γ-brass), and $Sm_{11}Cd_{45}$ structures.[1] We consider these six because either the structures themselves or more complex variants of them exhibit a common pseudo fivefold symmetry. The common pseudo fivefold axes lie along the ⟨110⟩ directions of the cubic unit

---

[a] R. F. Berger, Prof. S. Lee, J. Johnson, B. Nebgen, A. C.-Y. So
Department of Chemistry and Chemical Biology
Cornell University, Ithaca, NY 14853–1301 (USA)
Fax: (+1) 607-255-4137
E-mail: sl137@cornell.edu

Supporting information for this article is available on the WWW under http://dx.doi.org/10.1002/chem.200800336 or from the author.

[1] Several of the remaining structure types (e.g. Cr_3Si and YCd_6) are known to be quasicrystal approximants of 3D point group quasicrystals.[13,14]

cell, as opposed to the $\langle 1\tau 0\rangle$ directions of other known cubic quasicrystal approximants ($\tau=\frac{1+\sqrt{5}}{2}$).[15] Interestingly, although there are 3D point groups with fivefold axes along the $\langle 1\tau 0\rangle$ directions (e.g. the I_h point group), there are no 3D point groups with fivefold axes along the $\langle 110\rangle$ directions.

Earlier work by Sadoc and Mosseri[16,17] has shown that the $MgCu_2$, γ-brass, and α-Mn structures can be understood in terms of a 4D Platonic solid, the 600-cell. This finding helps rationalize the observed pseudo fivefold symmetry in these structures. The 600-cell, along with its dual, the 120-cell, are the 4D Platonic solids with the greatest number of symmetry elements (14400 in total).[18] Among these symmetries are numerous fivefold rotations. One type of projection, the 4D to 3D cell-projection (we explain cell-projection later in this paper), places six of these fivefold operations closest to the center of the projection. By virtue of being closest to the center, these six fivefold operations best preserve their fivefold pseudo-symmetry when projected into 3D.[2] The six projected pseudo fivefold axes lie exactly along the $\langle 110\rangle$ directions of a cube. Thus, the symmetry of the 600-cell can be used to account for the pseudo fivefold symmetry in the above structure types.[19]

One limitation of the above approach is that the 600-cell, for all its complexity, is still a finite polyhedroid,[3] whereas the structures of interest in this paper are extended crystals and are hence infinite in size. One way around this difficulty has been the introduction of disclination lines.[22,23] In this paper, we adopt an alternate approach. Rather than consider the 600-cell itself, we consider a 4D structure which has the same 4D point group as the 600-cell but which, like the crystal structures of interest, is infinite in size. This 4D object is the 4D quasicrystal first proposed by Elser and Sloane[24] and later studied by Moody, Patera, Sadoc, and Mosseri.[25,26]

The Elser–Sloane 4D quasicrystal, since its introduction in 1987, has lost favor to the now well-known 6D crystal to 3D quasicrystal model.[27–30] In the more widely used 6D to 3D model, as well as in all other quasicrystals and quasicrystal approximants of which we know, quasicrystals are rationalized by combining a 3D point group with higher dimensional translations. In this paper, by contrast, we find that rational approximants of the Elser–Sloane 4D quasicrystal, with its fundamentally higher dimensional point group, coupled with a 4D to 3D cell-projection (see below) can account for all the atomic positions of Be_5Au and all the *heavy* atom sites of $Li_{21}Si_5$,[31] $Sm_{11}Cd_{45}$,[11] and $Mg_{44}Ir_7$.[32,33] For the latter three structures, quasicrystal approximants of the Elser–Sloane quasicrystal account for respectively 10/12, 9/13, and 9/11 of the lighter atom sites.

These results are of particular interest as Be_5Au and $Li_{21}Si_5$ are themselves exact superstructures of two of the title compounds of this article: $MgCu_2$ (the cubic Laves phase) and Cu_5Zn_8 (γ-brass), respectively. Furthermore, $Sm_{11}Cd_{45}$ is a superstructure built up from the α-Mn structure coupled with bcc. It has been recently shown that $Mg_{44}Ir_7$ is nicely rationalized as being composed of twinned Ti_2Ni-type domains.[34] Both $Sm_{11}Cd_{45}$ and $Mg_{44}Ir_7$ belong to a family of superstructures (here termed $2\times 2\times 2$ superstructures for their usual description as arrays of "clusters" in large unit cells) first studied by Westman, Westin, and Samson. [11,31–33,35–47]

Although superstructures (Be_5Au, $Li_{21}Si_5$, $Sm_{11}Cd_{45}$, and $Mg_{44}Ir_7$) have the most enhanced pseudo fivefold symmetry along the $\langle 110\rangle$ directions, and which therefore connect best to the Elser–Sloane model, it seems fair to assume that their substructures ($MgCu_2$, Cu_5Zn_8, Ti_2Ni, and α-Mn) are also implicated in the Elser–Sloane model. With this Ansatz, the results of this paper suggest that four of the most common complex cubic metallic structures ($MgCu_2$, Be_5Au, Cu_5Zn_8, and $Sm_{11}Cd_{45}$) are all related to rational cell-projections of the 4D quasicrystal model. The results further tentatively suggest that an additional two common structure types (Ti_2Ni and α-Mn) are also so connected. We begin with the Laves phase $MgCu_2$ and its superstructure Be_5Au.

Results and Discussion

The cubic Laves structure—$MgCu_2$ and Be_5Au: The three most common binary intermetallic stoichiometries are 1:1, 1:2, and 1:3. Although the 1:1 and 1:3 stoichiometries are dominated by ordered variants of fcc, hcp, and bcc, the 1:2 stoichiometry's most common structures are Laves phases.[1] In this paper, we consider the cubic Laves structure $MgCu_2$. In $MgCu_2$, the Mg atoms lie in a diamond network (Figure 1a), whereas the Cu atoms form a network of vertex-sharing tetrahedra (Figure 1b). The full $MgCu_2$ structure is illustrated in Figure 1c.

The most common $MgCu_2$ superstructure is the Be_5Au type. In this superstructure, the network of vertex-sharing tetrahedra remains all one atom type (Be), but the original diamond network is replaced by an alternating network of the two atom types (Au and Be). The alternating network (Figure 1d) may be recognized as a sphalerite-like ordering of a diamond network. The vertex-sharing tetrahedra and the full Be_5Au structure are illustrated in Figure 1e,f.

Although the $MgCu_2$ and Be_5Au structures differ only in the type of atom lying at individual sites, and may be thought of as having very similar structures, their diffraction patterns are noticeably different. Be_5Au has marked pseudo tenfold diffraction symmetry (pseudo fivefold structural symmetry coupled with Friedel's Law[48]) along the $\langle 110\rangle$ directions; $MgCu_2$ does not. In Figure 2, we illustrate the calculated diffraction patterns[49] of both of these structures along [110]. The $MgCu_2$ diffraction pattern (Figure 2a) is a standard pattern with an immediately discernible rhomboid

---

[2] In 4D, fivefold rotations occur around invariant planes. If projected into 3D, they become pseudo fivefold rotations, and occur around invariant axes.

[3] A polyhedroid[20,21] is the 4D analog of a 3D polyhedron. Just as a polygon is composed of vertices and edges and a polyhedron consists of vertices, edges, and faces, a 4D polyhedroid has vertices, edges, faces, and polyhedra. These polyhedra are referred to as cells. The name 600-cell means that this polyhedroid contains 600 polyhedra.

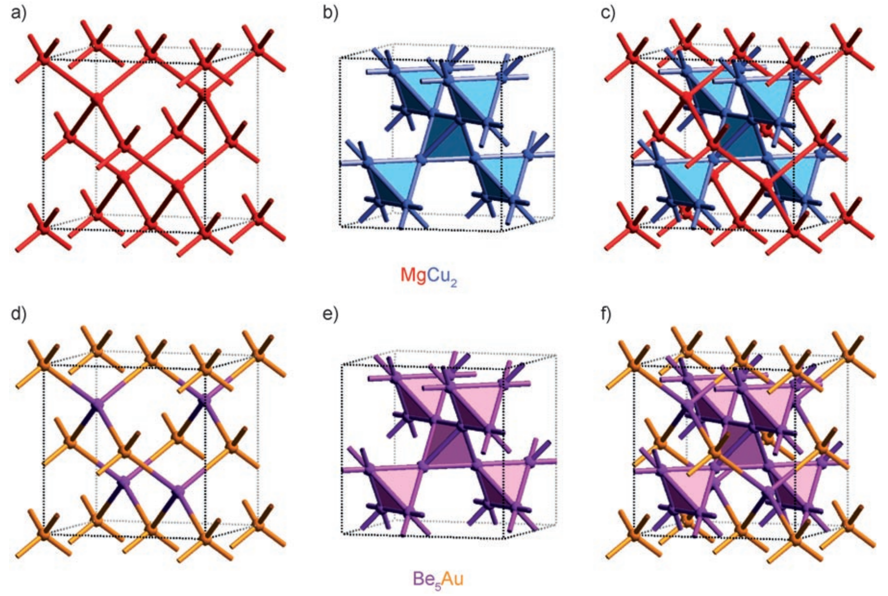

Figure 1. The cubic Laves structure $MgCu_2$ and its superstructure Be_5Au. a) A diamond network of Mg (red) atoms and b) a vertex-sharing tetrahedral network of Cu (blue) atoms combine to make c) the $MgCu_2$ structure. d) A diamond network of alternating Be (purple) and Au (orange) atoms and e) a vertex-sharing tetrahedral network of Be atoms that combine to make f) Be_5Au.

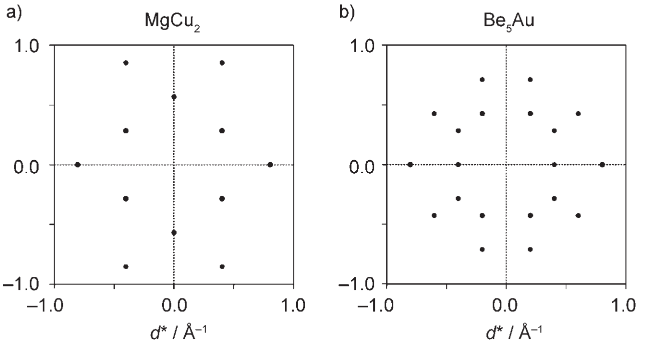

Figure 2. The strongest peaks in the [110] X-ray diffraction patterns[49] of the a) $MgCu_2$ and b) Be_5Au structures. The site preferences in the Be_5Au structure give it a pseudo tenfold diffraction symmetry that is absent in $MgCu_2$. The latter pattern was calculated using the isostructural compound UCu_5, a compound for which the pseudo-symmetry is particularly vivid.

reciprocal lattice. By contrast, the dominant diffraction peaks of the Be_5Au structure (Figure 2b) lie in two concentric rings, each composed of ten peaks. Given the constraint of the large reciprocal lattice (owing to the relatively small direct lattice vectors), it is noteworthy how well these two tenfold rings parse themselves to give an overall pseudo tenfold diffraction symmetry.

To understand the Be_5Au structure, we must rationalize its pseudo tenfold diffraction symmetry. In our hands, such a rationalization is based on a higher dimensional lattice, the E_8 lattice, which lies at the foundation of the Elser–Sloane quasicrystal model. Remarkably, this higher dimensional crystal lattice is 8D; our interest will be in 3D projections of it.

The E_8 lattice and its 3D cell-centered projection: When it comes to using the 4D 600-cell to generate 3D projected crystal structures, there is a major complication: the 600-cell 4D point group is not found in any 4D space groups. In this, it is entirely akin to the 3D I_h point group, which is not found in any 3D space groups. Just as in the I_h case, where one needs to extend to a higher dimension (6D is generally chosen[27–30]) to find a space group which contains I_h symmetry, we will extend into 8D in the case of the 600-cell point group.[24–26,50] In the former case, projection from a 6D crystalline lattice results in 3D I_h quasicrystals. In the latter case, Elser and Sloane have found that projection from an 8D crystalline lattice results in a 4D quasicrystal with 600-cell point group symmetry.[24]

The 8D lattice in question is the closest-packed E_8 lattice, with points of the types $(n_1, n_2, n_3, n_4, n_5, n_6, n_7, n_8)$ and $(n_1+\tfrac{1}{2}, n_2+\tfrac{1}{2}, n_3+\tfrac{1}{2}, n_4+\tfrac{1}{2}, n_4+\tfrac{1}{2}, n_6+\tfrac{1}{2}, n_7+\tfrac{1}{2}, n_8+\tfrac{1}{2})$. In both cases, the n_i are all integers *and* their sum is even (i.e. $\sum_{i=1}^{8} n_i = 2N$).[51] As the crystal structures discussed in this paper are of T_d point group symmetry, our interest will be in 3D projections of the E_8 lattice which preserve an overall 3D T_d symmetry. We adapt a procedure from our previous paper.

In this earlier work, we required a projection of the 4D 600-cell which placed a single tetrahedral cell at the center of the projection. In so doing, it preserved an overall T_d symmetry in the 3D projected atomic cluster. This specification—that the four 4D sites of a given 4D tetrahedral cell project to the four sites of a 3D tetrahedron—exactly determines all twelve matrix elements of the 3×4 projection matrix; it exactly determines what we term a cell projection. Applying this same 3×4 matrix to the remaining sites of the 600-cell generates the full 3D cell-projected 600-cell.[19]

Important to the current paper is that, just outside the central tetrahedron of the 3D cell-projected 600-cell, there is a second tetrahedron roughly 1.6 times larger in size. This larger tetrahedron is termed the outer tetrahedron (OT), and the smaller one the inner tetrahedron (IT). The eight vertices that comprise IT and OT are collectively known as a stella quadrangula (Figure 3a).[52,53] One feature of the stella quadrangula that will be key to our later discussion is that each OT site, together with the triangular IT face nearest to it, forms a capping tetrahedron (Figure 3b). These capping

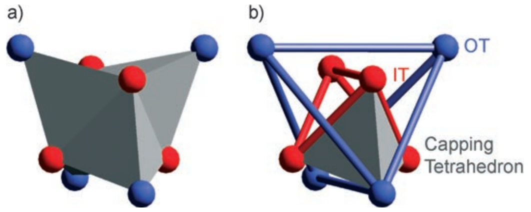

Figure 3. The 8-vertex formation known as a stella quadrangula. The vertices are shown as a) a single polyhedron, and b) an inner tetrahedron (IT, red) and an outer tetrahedron (OT, blue). Highlighted in gray in the latter view is a tetrahedron composed of three IT atoms and one OT atom, which caps the inner tetrahedron.

tetrahedra are perfectly regular in shape if OT is exactly τ times larger than IT.

The stella quadrangula is vital to the desired 8D to 3D projection, for which a 3×8 matrix rather than the previous 3×4 matrix is required. For 8D, we need to specify how eight, not four, sites project into 3D. The natural choice for these eight sites are those comprising the stella quadrangula—the four IT sites and the four OT sites. In order to choose which 8D points project onto this 3D stella quadrangula, we consider a stella quadrangula from the Elser–Sloane quasicrystal and determine the eight 8D points which project onto it. We find the points (1,0,0,0,1,0,0,0), (1,0,0,0,0,1,0,0), (1,0,0,0,0,0,1,0), and (1,0,0,0,0,0,0,1) project onto the IT of the stella quadrangula, whereas the points $({}^1\!/_2, {}^1\!/_2, {}^1\!/_2, {}^1\!/_2, {}^1\!/_2, {}^1\!/_2, {}^1\!/_2, {}^1\!/_2)$, $({}^1\!/_2, -{}^1\!/_2, -{}^1\!/_2, {}^1\!/_2, {}^1\!/_2, {}^1\!/_2, {}^1\!/_2, {}^1\!/_2)$, $({}^1\!/_2, -{}^1\!/_2, {}^1\!/_2, -{}^1\!/_2, {}^1\!/_2, {}^1\!/_2, {}^1\!/_2, {}^1\!/_2)$, and $({}^1\!/_2, {}^1\!/_2, -{}^1\!/_2, -{}^1\!/_2, {}^1\!/_2, {}^1\!/_2, {}^1\!/_2, {}^1\!/_2)$ project onto the OT.

We therefore require the following transormations (1–8):

$$(1, 0, 0, 0, 1, 0, 0, 0) \rightarrow (1, 1, 1) \tag{1}$$

$$(1, 0, 0, 0, 0, 1, 0, 0) \rightarrow (1, -1, -1) \tag{2}$$

$$(1, 0, 0, 0, 0, 0, 1, 0) \rightarrow (-1, 1, -1) \tag{3}$$

$$(1, 0, 0, 0, 0, 0, 0, 1) \rightarrow (-1, -1, 1) \tag{4}$$

$$({}^1\!/_2, {}^1\!/_2, {}^1\!/_2, {}^1\!/_2, {}^1\!/_2, {}^1\!/_2, {}^1\!/_2, {}^1\!/_2) \rightarrow (-t, -t, -t) \tag{5}$$

$$({}^1\!/_2, -{}^1\!/_2, -{}^1\!/_2, {}^1\!/_2, {}^1\!/_2, {}^1\!/_2, {}^1\!/_2, {}^1\!/_2) \rightarrow (t, -t, t) \tag{6}$$

$$({}^1\!/_2, -{}^1\!/_2, {}^1\!/_2, -{}^1\!/_2, {}^1\!/_2, {}^1\!/_2, {}^1\!/_2, {}^1\!/_2) \rightarrow (-t, t, t) \tag{7}$$

$$({}^1\!/_2, {}^1\!/_2, -{}^1\!/_2, -{}^1\!/_2, {}^1\!/_2, {}^1\!/_2, {}^1\!/_2, {}^1\!/_2) \rightarrow (t, t, -t) \tag{8}$$

Taking the above 8D and 3D points to be column vectors, the 3×8 matrix that performs these transformations is:

$$\begin{pmatrix} 0 & 0 & -2t & 0 & 1 & 1 & -1 & -1 \\ 0 & 0 & 0 & -2t & 1 & -1 & 1 & -1 \\ 0 & -2t & 0 & 0 & 1 & -1 & -1 & 1 \end{pmatrix}$$

The ${}^1\!/_1$ quasicrystal approximant

Projection matrix: Given a value of t, the above 3×8 matrix exactly defines the 8D to 3D projection. As we have noted above, if $t=\tau$, the resultant 3D stella quadrangula will have perfectly regular capping tetrahedra. But, as we will find below, for this value and indeed for any irrational value of t, the resultant 3D structure will be a quasicrystal. Rather than show this directly, we consider first several rational values of t.

We consider a sequence of rational numbers which converges to τ. The sequence chosen is composed of the ratios of consecutive members of the Fibonacci sequence (1, 1, 2, 3, 5, 8, ..). As can be seen by inspection, this sequence (${}^1\!/_1$, ${}^2\!/_1$, ${}^3\!/_2$, ${}^5\!/_3$, ${}^8\!/_5$, ..) converges rapidly to the desired value. We consider first $t={}^1\!/_1=1$. For this value, the 3×8 projection matrix reduces to:

$$\begin{pmatrix} 0 & 0 & -2 & 0 & 1 & 1 & -1 & -1 \\ 0 & 0 & 0 & -2 & 1 & -1 & 1 & -1 \\ 0 & -2 & 0 & 0 & 1 & -1 & -1 & 1 \end{pmatrix}$$

We consider now the three column vectors:

$$\mathbf{a} = \begin{pmatrix} 0 \\ 0 \\ -2 \\ 0 \\ 1 \\ 1 \\ -1 \\ -1 \end{pmatrix} \qquad \mathbf{b} = \begin{pmatrix} 0 \\ 0 \\ 0 \\ -2 \\ 1 \\ -1 \\ 1 \\ -1 \end{pmatrix} \qquad \mathbf{c} = \begin{pmatrix} 0 \\ -2 \\ 0 \\ 0 \\ 1 \\ -1 \\ -1 \\ 1 \end{pmatrix}$$

These three vectors are the transposed rows of the projection matrix. As can be directly verified, these three column vectors project onto respectively:

$$\vec{a} = \begin{pmatrix} 8 \\ 0 \\ 0 \end{pmatrix} \qquad \vec{b} = \begin{pmatrix} 0 \\ 8 \\ 0 \end{pmatrix} \qquad \vec{c} = \begin{pmatrix} 0 \\ 0 \\ 8 \end{pmatrix}$$

three orthogonal 3D vectors. As their names suggest, these three orthogonal vectors can be seen as three ordinary 3D unit cell axes.[4]

---

[4] In this paper, we adopt the nomenclature that bold-font **a** is an 8D vector, $\vec{a}$ is a 3D vector, and a is a scalar, the length of $\vec{a}$.

To cement this view, consider a given E_8 lattice point. Add to this 8D vector a linear combination of integer multiples of the 8D **a**, **b**, and **c** vectors. This addition will generate a new 8D vector corresponding to a new E_8 lattice point. Under the 8D to 3D projection, this new E_8 lattice point will project onto a 3D position related to the original projected 3D position by the same combination of $\vec{a}$, $\vec{b}$, and $\vec{c}$ as the initially chosen combination of **a**, **b**, and **c**. Therefore, $\vec{a}$, $\vec{b}$, and $\vec{c}$ can be taken to be standard 3D unit cell vectors.

Projected distances: The 3×8 matrix with $t={}^1\!/_1=1$ projects E_8 onto a 3D crystalline structure. However, this 3D structure by itself is not of great interest; it is merely bcc. More useful projections will be ones in which only a portion of the E_8 lattice is projected into 3D. To construct these, we require two additional concepts.

First is the concept of *projected distance*,[54] the distance between the original and projected coordinates. To explain what we mean by this, let us first illustrate projected distance in a simpler projection. In Figure 4a, we project a 2D square lattice onto a 1D line. This amounts to collapsing each lattice point perpendicularly onto the line (from the black circles to the cyan circles in the figure). The lengths of the red line segments are the *projected distances* of the points.

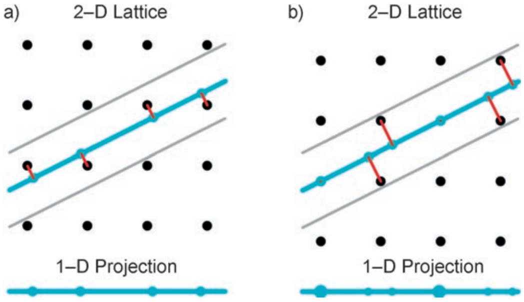

Figure 4. An illustration of projected distance and the effect of lattice translation, using the simpler projection of a 2D square lattice onto to 1D line. a) The points of a 2D square lattice project onto a 1D line (cyan) if they lie within a specified distance of that line (i.e. within the thinner gray lines). The lengths of the red line segments connecting the lattice points (black) to their projections (cyan) are what we define as projected distances. b) If the 2D lattice is translated downward and the same rule is applied, the result is a qualitatively different projection that includes points with varying projected distances.

The concept of projected distance is the same for our 8D to 3D projection; it is the distance from an 8D point to the 3D "slice" onto which it is projected. This can be defined formally as the perpendicular distance from an 8D point to the 3D span of the rows of the projection matrix. We will assume, as is standard, that sites which project over a shorter distance count more heavily in the final structure than those which project over a longer distance. At the bottom of Figure 4, we represent points with shorter projected distances using larger circles. Points which lie beyond a specified projected distance, denoted by the gray lines, are not projected at all.

This standard concept enriches the possibilities of 3D projected structures, in a way which we again illustrate using the simple 2D to 1D projection. In Figure 4b, the entire 2D square lattice is translated downward with respect to the 1D line of projection. This translation changes the projected distances of each point, moving some points closer to the line and others farther from it. The points that lie exactly on the line count more heavily in the projection than do the points farther from the line (and are consequently shown as larger circles at the bottom of Figure 4b). Thus, the translation of the lattice fundamentally alters the 1D projected structure by changing which points count most heavily in the projection.

This type of translation can be extended to the E_8 lattice in our projections. The E_8 lattice can be translated by an 8D vector **x**, which will determine which lattice points have the shortest projected distances, and thus count most heavily. All of the structure types on which we focus in this paper—$MgCu_2$, Be_5Au, Cu_5Zn_8, $Li_{21}Si_5$, Ti_2Ni, α-Mn, $Sm_{11}Cd_{45}$, and $Mg_{44}Ir_7$—have centers of T_d point group symmetry. Our interest is therefore in vectors **x** that leave the T_d symmetry of the stella quadrangula unchanged. We must explore all **x** that maintain the equal projected distances of the four IT sites as well as the four OT sites. Some thought shows that vectors of the type (x_1, 0, 0, 0, x_2, x_2, x_2, x_2) preserve the above equalities. There are therefore two free independent variables within the framework of $t={}^1\!/_1=1$ projection: x_1 and x_2.

Generating the Be₅Au structure: We now apply the $t={}^1\!/_1=1$ model to the Be_5Au structure. Be_5Au is a fully ordered structure, with 4 Au atoms and 20 Be atoms in its cubic unit cell. This brings us to the second concept required to fully specify a projection. If we wish to replicate the Be_5Au structure through projection, we must make a rule deciding which E_8 lattice points project as Au atoms and which as Be atoms. Our rule is as follows: for a given projection (corresponding to a pair of values x_1 and x_2), we take the 4 lattice points with the shortest projected distances to be Au atoms (the heavier element), and the next 20 points to be Be atoms (the lighter element). All sites with projected distances longer than these 24 will remain unoccupied. In this way, we ensure that our projections have the desired population and stoichiometry.

Given this rule, we can now generate a 3D crystal structure corresponding to any pair of values x_1 and x_2. Naturally, some of these structures will be more similar to the experimental Be_5Au structure than others. In Figure 5, we quantitatively assess how well each projection matches the Be_5Au structure. For given pairs of x_1 and x_2 parameters, we plot the total number of projected atoms that exactly correspond (including atom type) to the 24 experimental atoms. That is, we plot the number of projected Au atoms that exactly correspond to the 4 experimental Au atoms *plus* the number of

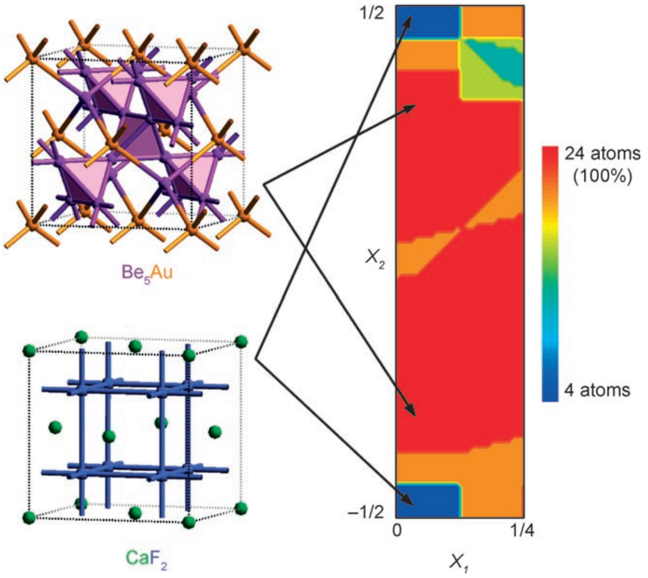

Figure 5. Correspondence between $^1/_1$ projected structures and the experimental Be$_5$Au structure as a function of x_1 and x_2, for a region containing all unique projected structures. The plot shows the number of atoms in the projected unit cell whose positions and elements exactly match those of experimental Be$_5$Au. There are substantial regions (shown in red) in which the match is perfect. In other regions, the projection perfectly matches the experimental CaF$_2$ structure.

projected Be atoms that exactly correspond to the 20 experimental Be atoms.

The red regions in Figure 5 represent projections in which *all* 4 Au atoms and *all* 20 Be atoms exactly correspond to those in the experimental Be$_5$Au structure. As we can see, there are substantial regions in which the match between projected and experimental crystal structure is perfect. These results suggest that the Be$_5$Au structure can be profitably taken to be a rational projection of the E_8 lattice. And as Be$_5$Au is an exact superstructure of the cubic Laves phase MgCu$_2$ structure, the parent structure itself can also be so understood.

Before leaving our analysis of Figure 5, it is worth examining some of the values of x_1 and x_2 which lead to structures other than the Be$_5$Au structure. As the blue regions of the Figure suggest, a very different structure emerges near the values of $x_1 = 0$ and $x_2 = ^1/_2$. This projected structure proves to be the CaF$_2$ structure type. As Figure 5 illustrates, it consists of an fcc lattice of the heavier element (the Ca site) which has all its tetrahedral holes filled by the lighter element (the F sites). An examination of known intermetallic CaF$_2$ compounds confirms that the Ca and F sites are generally occupied by respectively the heavier and the lighter metallic elements.[1]

γ-brass and the Li$_{21}$Si$_5$ structure: The cubic unit cell of Cu$_5$Zn$_8$ (γ-brass), with 52 atoms, is roughly twice the size of those of the MgCu$_2$ and Be$_5$Au structures. It is composed of a body-centered arrangement of two identical 26-atom clusters, which are based on the stella quadrangula. As we show in Figure 6, the stella quadrangula has two types of edges; those that link IT atoms to each other, and those that link IT to OT atoms. Capping each of the IT–IT edges with an atom generates an octahedron, referred to as OH (Figure 6a). Similarly, capping the twelve IT–OT edges generates a distorted cubo-octahedron, referred to as CO (Figure 6b). The resulting edge-capped stella quadrangula (Figure 6c, left) has 26 vertices (IT+OT+OH+CO=4+4+6+12=26), and is completely equivalent to the γ-brass cluster. On the right side of Figure 6c, we show a second view of the γ-brass cluster, which is more suggestive of the experimental site preferences in Cu$_5$Zn$_8$. The OT and OH sites, which are occupied by Cu atoms in Cu$_5$Zn$_8$, are connected as a black adamantane-like cage. The IT and CO sites, which are occupied by Zn, are connected as a light gray network of vertex-sharing tetrahedra. There are two of these 26-atom clusters

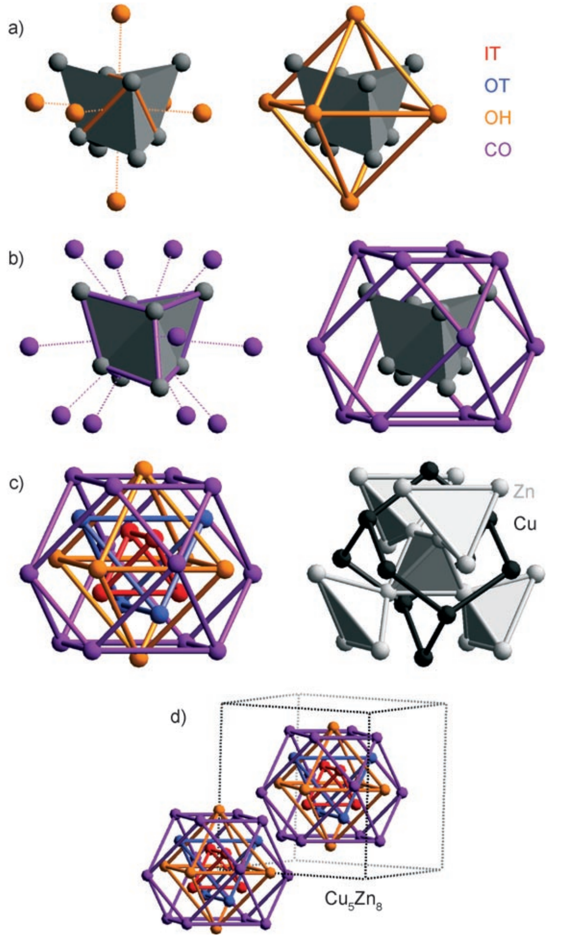

Figure 6. The construction of an edge-capped stella quadrangula, alternatively known as a γ-brass cluster. a) One type of edge of the stella quadrangula is capped with atoms (orange) that form an octahedron (OH), whereas b) the other type of edge is capped with atoms (purple) that form a distorted cubo-octahedron (CO). c) The full 26-atom edge-capped stella quadrangula can be seen as four nested polyhedra (left), or alternatively as an adamantane-like cage (right, black) and a network of vertex-sharing tetrahedra (right, light gray). d) The cubic unit cell of Cu$_5$Zn$_8$ contains two such identical clusters in a body-centered arrangement.

in the 52-atom cubic unit cell of Cu_5Zn_8, as shown in Figure 6d.

Our concern here will be with the γ-brass superstructure $Li_{21}Si_5$.[31] This superstructure is significantly larger than the parent structure and has 16 γ-brass clusters in its cubic unit cell. The unit cell has an a-axis length of 18.710 Å, contains 416 atoms, and has a face-centered cubic Bravais lattice. The 16 γ-brass clusters in this structure reduce to four crystallographically inequivalent clusters. It is convenient to consider the four clusters along the body diagonal of the cubic unit cell as representative examples of each crystallographically inequivalent cluster.

These four clusters are illustrated in Figure 7. For the sake of clarity, each is connected as an adamantane-like cage and a network of vertex-sharing tetrahedra (as illustrated on the right side of Figure 6c). Each cluster is given a specific name. The cluster centered at (0,0,0) is labeled Z for zero. Similarly, clusters centered at $(^1/_4, ^1/_4, ^1/_4)$, $(^1/_2, ^1/_2, ^1/_2)$, and $(^3/_4, ^3/_4, ^3/_4)$ are respectively called Q, H, and T (for quarter, half, and three-quarters).

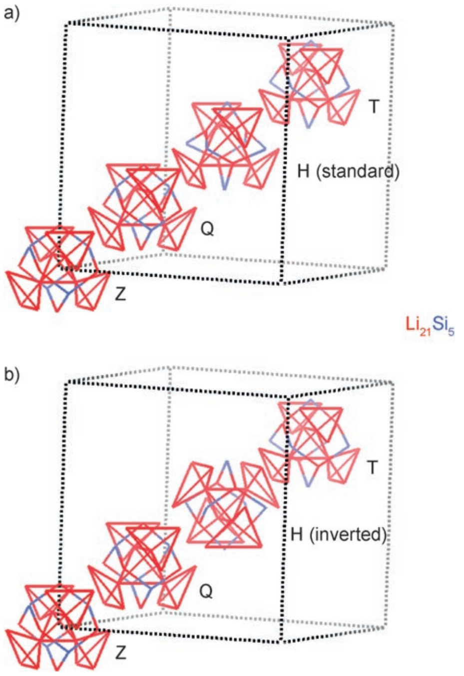

Figure 7. The four crystallographically inequivalent γ-brass clusters in the cubic unit cell of $Li_{21}Si_5$. The four Si (blue) sites are ZOT, QOT, HOH, and TOH, whereas the remaining twelve sites are Li (red). The H cluster is shown in a) the same orientation as the others, and in b) an inverted orientation. The latter picture is more indicative of experimental atomic positions.

$Li_{21}Si_5$ is a fully atomically ordered variant of the γ-brass structure. The OT sites of both the Z and Q clusters are occupied by Si atoms, as are the OH sites of the H and T clusters. We refer to the four Si sites as respectively ZOT, QOT, HOH, and TOH. The atomic ordering is illustrated in Figure 7. It is of interest that different sites are occupied by Si atoms: some are OT whereas others are OH.

Figure 7a shows a standard illustration of $Li_{21}Si_5$ with all four crystallographically inequivalent clusters oriented the same way. This standard view obfuscates one remarkable feature of the structure. Although three of the four clusters in the $Li_{21}Si_5$ structure are typical γ-brass clusters, the inner tetrahedron of the H cluster is *larger* than the outer tetrahedron of the same cluster.[31]

If we assume that inner tetrahedra should perforce be smaller than outer tetrahedra, we need to switch the atomic labels of these two sites. As shown in Figure 7b, it is possible to switch these labels and retain the overall edge-capped stella quadrangular geometry if we invert the entire H cluster. Thus, although one can describe $Li_{21}Si_5$ as a $2\times2\times2$ superstructure of γ-brass with all four γ-brass clusters oriented the same way, it is perhaps more atomically accurate to view this structure as a superstructure where three of the clusters have one orientation and the fourth cluster is inverted.

Just as in the case of Be_5Au and $MgCu_2$, the $Li_{21}Si_5$ superstructure has enhanced pseudo tenfold diffraction symmetry along $\langle 110 \rangle$ compared to the Cu_5Zn_8 parent structure. The two diffraction patterns are contrasted in Figure 8. As can be seen, the pseudo tenfold diffraction of the $Li_{21}Si_5$ structure is quite marked. With its larger direct lattice cell and consequent smaller reciprocal lattice cell, the parsing of the 10 concentric diffraction peaks is distinctly superior to what was found for Be_5Au.

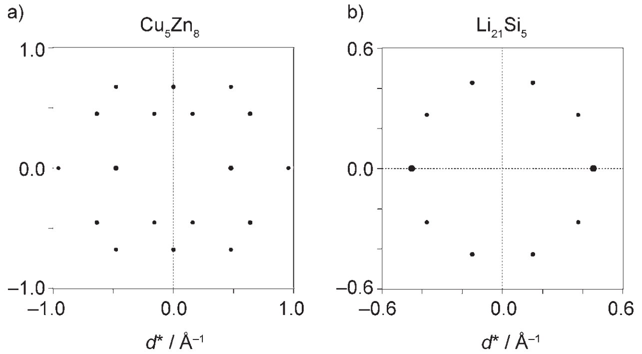

Figure 8. The strongest peaks in the [110] X-ray diffraction patterns[49] of the a) Cu_5Zn_8 and b) $Li_{21}Si_5$ structures. The site preferences in $Li_{21}Si_5$ give it a pseudo tenfold diffraction symmetry that is absent in Cu_5Zn_8.

The $^2/_1$ *quasicrystal approximant*: In an approach similar to that taken for the Be_5Au structure, we wish to show the connection between the $Li_{21}Si_5$ structure and the E_8 lattice. Its more complicated structure will require a few refinements to the overall procedure. In Be_5Au, all the atoms reside at positions of high symmetry, none of which contain any free atomic parameters. By contrast, in $Li_{21}Si_5$, there are 4 crystallographically inequivalent heavy atom sites and 12 inequivalent light atom sites with a combined 20 atomic parameters.

Our goal will be to project the E_8 lattice points near the experimentally observed atomic sites in $Li_{21}Si_5$. As we shall see, we will find a projection which locates all 4 inequivalent heavy atom sites and 10 of the 12 inequivalent light atom sites. Moreover, this optimal structure will have three clusters with one orientation, and the H cluster correctly inverted.

For $Li_{21}Si_5$, we apply a 3×8 projection matrix where $t={}^{2}\!/_{1}=2$:

$$\begin{pmatrix} 0 & 0 & -4 & 0 & 1 & 1 & -1 & -1 \\ 0 & 0 & 0 & -4 & 1 & -1 & 1 & -1 \\ 0 & -4 & 0 & 0 & 1 & -1 & -1 & 1 \end{pmatrix}$$

Similarly to the previous case, the three transposed rows of this matrix form the three 8D vectors:

$$\mathbf{a}=\begin{pmatrix} 0 \\ 0 \\ -4 \\ 0 \\ 1 \\ 1 \\ -1 \\ -1 \end{pmatrix} \quad \mathbf{b}=\begin{pmatrix} 0 \\ 0 \\ 0 \\ -4 \\ 1 \\ -1 \\ 1 \\ -1 \end{pmatrix} \quad \mathbf{c}=\begin{pmatrix} 0 \\ -4 \\ 0 \\ 0 \\ 1 \\ -1 \\ -1 \\ 1 \end{pmatrix}$$

which project onto the three orthogonal 3D cell axis vectors:

$$\vec{a}=\begin{bmatrix} 20 \\ 0 \\ 0 \end{bmatrix} \quad \vec{b}=\begin{bmatrix} 0 \\ 20 \\ 0 \end{bmatrix} \quad \vec{c}=\begin{bmatrix} 0 \\ 0 \\ 20 \end{bmatrix}$$

Just as in the previous case, the E_8 lattice is subject to an 8D translation by the vector **x**. In order to retain the T_d symmetry of the projection, **x** must again be of the form (x_1, 0, 0, 0, x_2, x_2, x_2, x_2), with the two free parameters x_1 and x_2. In Figure 9, we plot the agreement between the projected structure and the experimental $Li_{21}Si_5$ structure as a function of these two parameters. Noting the 18.710 Å a-axis length of the experimental structure, we assume that projected atoms which lie within 1 Å of the actual atomic position are reasonably near the atomic position. As we shall see, most of the projected sites will lie significantly closer than the assumed 1 Å cut-off (with an average of 0.55 Å over the 16 distinct sites in experimental $Li_{21}Si_5$).

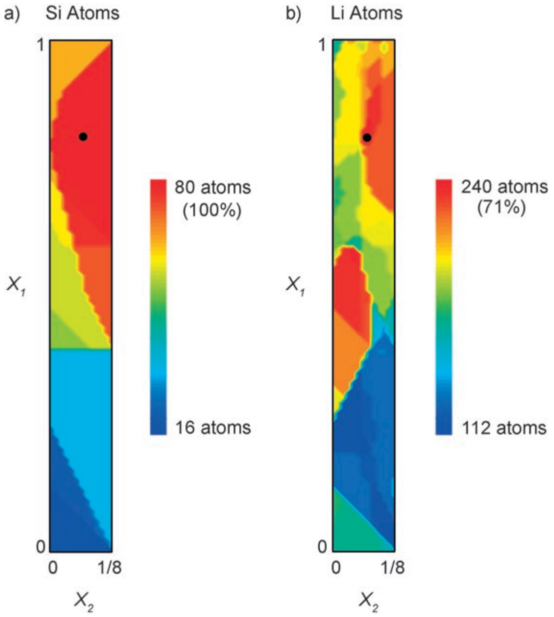

Figure 9. Correspondence between ${}^{2}\!/_{1}$ projected structures and the experimental $Li_{21}Si_5$ structure as a function of x_1 and x_2, for a region containing all unique projected structures. The plots show a) the number of projected Si atoms within 1 Å of experimental Si atoms, and b) the number of projected Li atoms within 1 Å of experimental Li atoms. The black dots indicate the optimal projection ($x_1=0.81$, $x_2=0.07$), for which 100 % of the Si atoms and 71 % of the Li atoms are correctly placed.

As Figure 9 shows, when $x_1=0.81$ and $x_2=0.07$, all 80 Si atoms and 240 of the 336 Li atoms can be located. This corresponds to the correct determination of all 4 Si and 10 of the 12 Li crystallographically inequivalent sites. In Table 1, all experimentally observed atomic sites are compared to their projected counterparts. Also given in this table are the projected distances of each of these sites for the optimal values of x_1 and x_2. A full account of this theoretical model is given in Table 1 of the Supporting Information, which shows not only the sites that are found experimentally, but all sites in our theoretical projection.

Two features of the projected E_8 model are noteworthy. First, the projected model correctly finds that half the OT and half the OH sites are occupied by Si atoms. The ordering of the four clusters is the experimental one, with ZOT, QOT, HOH, and TOH being the four Si sites. Equally noteworthy is the success in generating the H cluster. All four crystallographically inequivalent H sites are contained in the optimal projected E_8 model (though one lies slightly beyond the 1 Å cut-off). These four sites belong to a cluster which is inverted with respect to the other three clusters. As we discussed above, this inversion is found experimentally.

Although all the Si atoms are correctly determined, only 71 % of the experimental Li atoms are correctly found. As Table 1 shows, one of the missing sites (HCO) lies just beyond the established 1 Å cut-off (at 1.18 Å), whereas the other (QCO) lies just beyond the projected distance cutt-

Table 1. The calculated atomic sites (in fractional coordinates of the cubic unit cell) in the $^2/_1$ projection centered at (0.81,0,0,0,0.07,0.07,0.07,0.07), which match the experimental sites in $Li_{21}Si_5$.

Theoretical coordinates	Theor element	Proj distance	Experimental coordinates	Exptl element	Exptl site name	Exptl/proj separation [Å]
(0.95,0.75,0.75)	Si	0.51	(0.9280,0.7500,0.7500)	Si	TOH	0.41
(0.35,0.35,0.35)	Si	0.52	(0.3325,0.3325,0.3325)	Si	QOT	0.57
(0.70,0.50,0.50)	Si	0.60	(0.6809,0.5000,0.5000)	Si	HOH	0.36
(0.10,0.10,0.10)	Si	0.61	(0.0905,0.0905,0.0905)	Si	ZOT	0.31
(0.20,0.00,0.00)	Li	0.80	(0.1770,0.0000,0.0000)	Li	ZOH	0.43
(0.55,0.55,0.55)	Li	0.81	(0.5620,0.5620,0.5620)	Li	HIT	0.39
(0.95,0.95,0.95)	Li	0.81	(0.9460,0.9460,0.9460)	Li	ZIT	0.13
(0.15,0.15,0.95)	Li	0.82	(0.1580,0.1580,0.9880)	Li	ZCO	0.74
(0.70,0.70,0.70)	Li	0.88	(0.6910,0.6910,0.6910)	Li	TIT	0.29
(0.90,0.90,0.70)	Li	0.88	(0.9030,0.9030,0.7290)	Li	TCO	0.55
(0.45,0.25,0.25)	Li	0.99	(0.4240,0.2500,0.2500)	Li	QOH	0.49
(0.85,0.85,0.85)	Li	0.99	(0.8330,0.8330,0.8330)	Li	TOT	0.55
(0.40,0.40,0.40)	Li	1.02	(0.4210,0.4210,0.4210)	Li	HOT	0.68
(0.20,0.20,0.20)	Li	1.02	(0.1790,0.1790,0.1790)	Li	QIT	0.68
(0.65,0.65,0.55)	$^1/_2$ Li	1.02	(0.6620,0.6620,0.4890)	Li	HCO	1.18
(0.40,0.40,0.20)	–	1.03	(0.4140,0.4140,0.2500)	Li	QCO	1.01

off, beyond which atoms do not project (1.03 vs. 1.02). A more complete understanding of the projected model of $Li_{21}Si_5$ can be obtained from Table 1 of the Supporting Information. As this complete list of projected sites shows, there is a clear trend of shorter projected distances where atoms are found experimentally, and longer projected distances where atoms are not found. Of the 22 sites that are predicted theoretically by our optimal model of $Li_{21}Si_5$, 15 are analogs of sites that are found experimentally. Of the 34 sites that lie beyond this optimal projection, and are thus *not* predicted theoretically, 33 are *not* the analogs of experimental sites.

When looking at the discrepancies between the theoretical and experimental structures, it seems reasonable to assume that ordinary chemical constraints—atomic size, electronic structure, electronegativity, valence electron count, and quantum mechanics in general—should play a role in the structural energetics, and would thus modify the established "rules" for projection. We attribute the differences between the theoretical and experimental structures to such factors.

$Sm_{11}Cd_{45}$, $Mg_{44}Ir_7$, Ti_2Ni, and α-Mn: We turn now to the $Sm_{11}Cd_{45}$ and $Mg_{44}Ir_7$ structures. Both structures have excellent pseudo tenfold diffraction symmetry along ⟨110⟩, as shown in Figure 10. Both structures are ordered *F*-centered cubic structures with more than 400 atoms in their unit cells. Similarly to $Li_{21}Si_5$, their structures consist of four crystallographically inequivalent clusters centered at the Z, Q, H, and T positions. In $Sm_{11}Cd_{45}$, two clusters are based on the α-Mn structure, and two on bcc. In $Mg_{44}Ir_7$, clusters are derived from Ti_2Ni, γ-brass, and α-Mn.[55] We first turn to the new cluster types found in this pair of structures.

Three new cluster types need to be delineated: the α-Mn, Ti_2Ni, and bcc clusters. In Figure 11, we illustrate these three new cluster types. Site names used in describing γ-brass can also be used for the Ti_2Ni cluster (Figure 11a). For α-Mn and bcc (Figure 11b,c), however, in addition to the previously discussed site types, two new sites are also found: the cluster center (CC) and the truncated tetrahedron (TT). In Figure 12, we illustrate the crystallographically inequivalent clusters of $Sm_{11}Cd_{45}$ and $Mg_{44}Ir_7$ using the nomenclature derived in Figure 7.

The heavy atoms of these two structures occupy a mishmash of site types. The Sm sites in $Sm_{11}Cd_{45}$ are ZCC, ZCO, QCC, HOT, and TOT, whereas the Ir sites in $Mg_{44}Ir_7$ are ZOT, QOT, and TOH. In all, four different site types—CC, OT, OH and CO—are occupied by heavier atoms.

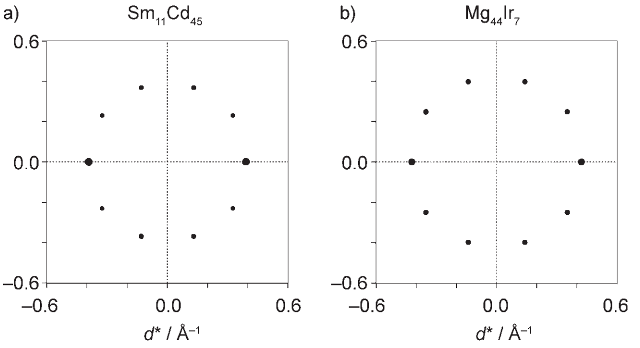

Figure 10. The strongest peaks in the [110] X-ray diffraction patterns[49] of the a) $Sm_{11}Cd_{45}$ and b) $Mg_{44}Ir_7$ structures. Similarly to the structures we have already generated by projection, these two exhibit a pseudo tenfold diffraction symmetry.

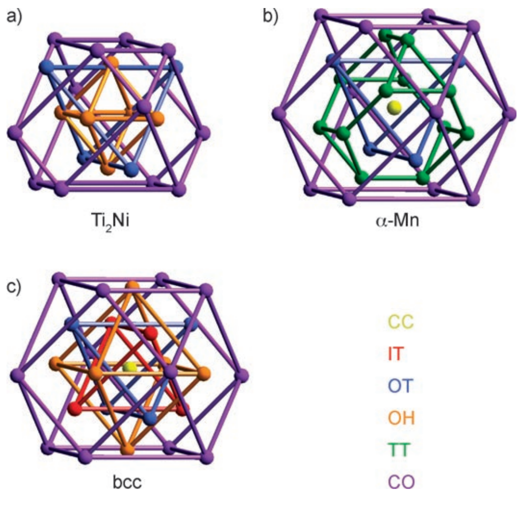

Figure 11. The a) Ti_2Ni, b) α-Mn, and c) body-centered cubic atomic clusters, connected as polyhedra according to their crystallographically inequivalent sites. In all, the clusters include six types of sites, which we abbreviate using two-letter names: CC (yellow), IT (red), OT (blue), OH (orange), TT (green), and CO (purple).

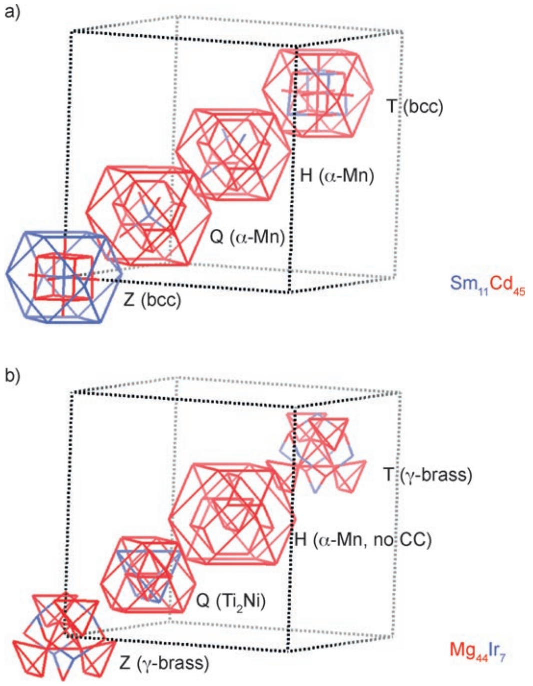

Figure 12. The four crystallographically inequivalent atomic clusters in the cubic unit cells of a) $Sm_{11}Cd_{45}$ and b) $Mg_{44}Ir_7$. In both cases, the heavier element is shown in blue, and the lighter element in red. The five Sm sites in $Sm_{11}Cd_{45}$ are ZCC, ZCO, QCC, HOT, and TOT, and the three Ir sites in $Mg_{44}Ir_7$ are ZOT, QOT, and TOH.

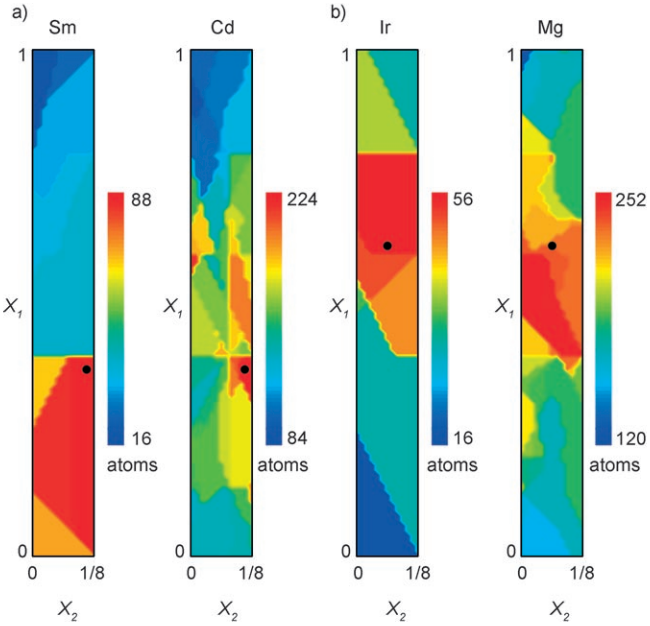

Figure 13. Correspondence between $^2/_1$ projected structures and the experimental a) $Sm_{11}Cd_{45}$ and b) $Mg_{44}Ir_7$ structures as functions of x_1 and x_2. In both panels, the plots show the number of projected heavy atoms within 1 Å of experimental heavy atoms (left), and the number of projected light atoms within 1 Å of experimental light atoms (right). The black dots indicate the optimal projection for each structure. For $Sm_{11}Cd_{45}$, the optimal point ($x_1 = 0.36$, $x_2 = 0.11$) correctly places 100 % of the Sm atoms and 62 % of the Cd atoms. For $Mg_{44}Ir_7$, the optimal point ($x_1 = 0.61$, $x_2 = 0.06$) correctly places 100 % of the Ir atoms and 66 % of the Mg atoms.

We turn now to $t = {}^2/_1 = 2$ models of the two structures. With the same approach as was previously used for $Li_{21}Si_5$, we plot the agreement between calculated and experimentally observed atomic sites for both the heavy and light atoms in $Sm_{11}Cd_{45}$ and $Mg_{44}Ir_7$ (Figure 13). For the former system and the values $x_1 = 0.36$ and $x_2 = 0.11$, all 88 Sm atoms (all 5 crystallographically inequivalent Sm sites) and 224 of the 360 Cd atoms (9 of 13 Cd sites) are correctly located. For $Mg_{44}Ir_7$, optimal agreement occurs when $x_1 = 0.61$ and $x_2 = 0.06$, when all 56 Ir atoms (all 3 crystallographically inequivalent Ir sites) and 232 of 352 Mg atoms (9 of 11 Mg sites) are successfully found. Tables 2 and 3 compare the projected and experimental atomic sites in $Sm_{11}Cd_{45}$ and $Mg_{44}Ir_7$, respectively.

The accuracy of these models is comparable to what was found for $Li_{21}Si_5$. All heavy atoms and 60–70 % of light atoms are correctly located in the best projections for each structure. It is noteworthy that the projected E_8 models correctly account for the unusual mixture of CC, OT, OH, and CO sites occupied by the heavier elements.

Complete lists of the all the sites generated by our optimal $Sm_{11}Cd_{45}$ and $Mg_{44}Ir_7$ projections are given in Table 2 and Table 3 of the Supporting Information. As in the case of

Table 2. The calculated atomic sites (in fractional coordinates of the cubic unit cell) in the $^2/_1$ projection centered at (0.36,0,0,0,0.11,0.11,0.11,0.11), which match the experimental sites in $Sm_{11}Cd_{45}$.

Theoretical coordinates	Theor element	Proj distance	Experimental coordinates	Exptl element	Exptl site name	Exptl/proj separation [Å]
(0.00,0.00,0.00)	Sm	0.42	(0.0000,0.0000,0.0000)	Sm	ZCC	0.00
(0.25,0.25,0.25)	Sm	0.46	(0.2500,0.2500,0.2500)	Sm	QCC	0.00
(0.40,0.40,0.40)	Sm	0.47	(0.4059,0.4059,0.4059)	Sm	HOT	0.22
(0.65,0.65,0.65)	Sm	0.50	(0.6618,0.6618,0.6618)	Sm	TOT	0.44
(0.20,0.20,0.00)	Sm	0.76	(0.1735,0.1735,0.0142)	Sm	ZCO	0.87
(0.45,0.45,0.25)	Cd	0.78	(0.4377,0.4377,0.2627)	Cd	QCO	0.47
(0.90,0.90,0.80)	Cd	0.79	(0.9161,0.9161,0.7637)	Cd	TCO	0.93
(0.75,0.75,0.75)	Cd	0.80	(0.7500,0.7500,0.7500)	Cd	TCC	0.00
(0.20,0.00,0.00)	Cd	0.81	(0.1573,0.0000,0.0000)	Cd	ZOH	0.93
(0.15,0.15,0.15)	Cd	0.83	(0.1636,0.1636,0.1636)	Cd	QOT	0.51
(0.50,0.50,0.50)	Cd	0.86	(0.5000,0.5000,0.5000)	Cd	HCC	0.00
(0.90,0.90,0.90)	Cd	0.88	(0.9126,0.9126,0.9126)	Cd	ZOT	0.47
(0.85,0.85,0.85)	Cd	0.98	(0.8297,0.8297,0.8297)	Cd	TIT	0.76
(0.30,0.30,0.40)	Cd	1.01	(0.2958,0.2958,0.3904)	Cd	QTT	0.24
(0.55,0.55,0.65)	–	1.02	(0.5455,0.5455,0.6403)	Cd	HTT	0.25
(0.05,0.05,0.05)	–	1.04	(0.0834,0.0834,0.0834)	Cd	ZIT	1.26
(0.95,0.75,0.75)	–	1.06	(0.9105,0.7500,0.7500)	Cd	TOH	0.86
(0.70,0.70,0.50)	–	1.07	(0.6728,0.6728,0.5128)	Cd	HCO	0.88

Table 3. The calculated atomic sites (in fractional coordinates of the cubic unit cell) in the $^2/_1$ projection centered at (0.61,0,0,0,0.06,0.06,0.06,0.06), which match the experimental sites in $Mg_{44}Ir_7$.

Theoretical coordinates	Theor element	Proj distance	Experimental coordinates	Exptl element	Exptl site name	Exptl/proj separation [Å]
(0.35,0.35,0.35)	Ir	0.42	(0.3482,0.3482,0.3482)	Ir	QOT	0.06
(0.10,0.10,0.10)	Ir	0.55	(0.0839,0.0839,0.0839)	Ir	ZOT	0.56
(0.95,0.75,0.75)	Ir	0.61	(0.9133,0.7500,0.7500)	Ir	TOH	0.74
(0.15,0.15,0.95)	Mg	0.76	(0.1561,0.1561,0.9797)	Mg	ZCO	0.62
(0.90,0.90,0.70)	Mg	0.84	(0.9015,0.9015,0.7194)	Mg	TCO	0.39
(0.20,0.00,0.00)	Mg	0.86	(0.1814,0.0000,0.0000)	Mg	ZOH	0.37
(0.55,0.55,0.55)	Mg	0.88	(0.5623,0.5623,0.5623)	Mg	HOT	0.43
(0.95,0.95,0.95)	Mg	0.88	(0.9482,0.9482,0.9482)	Mg	ZIT	0.06
(0.70,0.70,0.70)	Mg	0.95	(0.6973,0.6973,0.6973)	Mg	TIT	0.09
(0.70,0.70,0.50)	Mg	0.96	(0.6928,0.6928,0.4799)	Mg	HCO	0.45
(0.85,0.85,0.85)	Mg	0.97	(0.8338,0.8338,0.8338)	Mg	TOT	0.56
(0.40,0.40,0.20)	$^1/_{12}$ Mg	0.97	(0.3933,0.3933,0.2147)	Mg	QCO	0.35
(0.55,0.55,0.35)	–	0.99	(0.5517,0.5517,0.3385)	Mg	HTT	0.24
(0.35,0.25,0.25)	–	1.09	(0.3561,0.2500,0.2500)	Mg	QOH	0.12

$Li_{21}Si_5$, these lists show a clear trend of shorter projected distances where atoms are found experimentally, and longer projected distances where atoms are not found. In the optimal theoretical models of both $Sm_{11}Cd_{45}$ and $Mg_{44}Ir_7$, 37 sites lie beyond the projections and are thus *not* predicted theoretically. Comparing these two theoretical models to experiment, respectively 33 and 35 of those theoretically empty sites are correctly *not* the analogs of experimental atomic sites.

The possibility of a new quasicrystal: We have invoked many non-closest-packed cubic structures in this paper: $MgCu_2$, Be_5Au, Cu_5Zn_8 (γ-brass), $Li_{21}Si_5$, Ti_2Ni, α-Mn, $Sm_{11}Cd_{45}$, and $Mg_{44}Ir_7$. All of these structures are connected to 3D cell-projections of the E_8 lattice. If such quasicrystal approximants are so readily found, one might suppose that an actual cell-projected quasicrystal could also be eventually discovered. To aid in its potential search, let us detail what we may infer about such a quasicrystal.

By extension of the mathematics we considered above, such a quasicrystal will be based on the 3×8 matrix:

$$\begin{pmatrix} 0 & 0 & -2t & 0 & 1 & 1 & -1 & -1 \\ 0 & 0 & 0 & -2t & 1 & -1 & 1 & -1 \\ 0 & -2t & 0 & 0 & 1 & -1 & -1 & 1 \end{pmatrix}$$

For all rational values of t, including those already considered, one finds quasicrystal approximants. Only if t is an irrational number does projection lead to a non-crystal. The most interesting irrational value of t is τ. Here, each capping tetrahedron consisting of an OT atom and its three neighboring IT atoms is perfectly regular in shape. As the structures discussed above are all variants of tetrahedral packing, domains of such perfectly regular tetrahedra may be quite desirable.

The quasicrystal approximants discussed in this paper have elements vastly different in size. Let us assume that any potential quasicrystal will also contain at least two such dissimilar elements. In this paper, we have fared better in correctly locating the heavier of the elements. For the three $t={}^2/_1=2$ models discussed above, the heavier atoms were all correctly located, and had projected distances no longer than 0.61, 0.76, and 0.61 units of the E_8 lattice. Let us suppose that in an eventual quasicrystal, heavy atoms will be the E_8 vertices with projected distances shorter than 0.70.

What does such a structure look like? First, for a true quasicrystal, we no longer need consider the translation vector **x**. The quasicrystal remains unchanged for different values of this vector. We therefore need only consider a single structure. Different approaches have been chosen in the literature for the graphical representation of quasicrystals. In this paper, we choose a highly local view. In Figure 14, we provide local views of the quasicrystal around three particularly pseudo-symmetric positions. These views are directly compared with the heavy atom positions found in the various $t={}^2/_1=2$ quasicrystal approximants. Figure 14a shows one region of heavy atoms in this quasicrys-

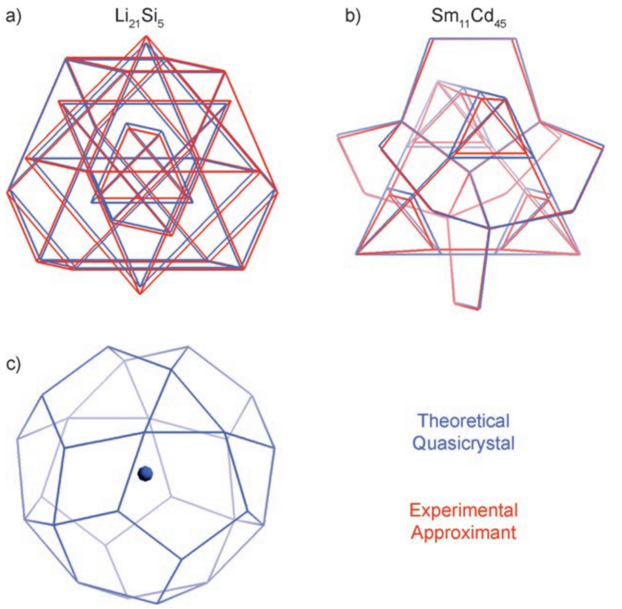

Figure 14. Correspondence between heavy atom positions in the proposed quasicrystal and its experimental approximants. a) Some regions in the quasicrystal resemble the pattern of heavy atoms in $Li_{21}Si_5$ (and $Mg_{44}Ir_7$), whereas b) others resemble the pattern of heavy atoms in $Sm_{11}Cd_{45}$. c) Still other regions in the proposed quasicrystal bear no such resemblance.

talline projection. As shown, these sites match closely with those of the 26 Si atoms closest to $(^1/_4, ^1/_4, ^1/_4)$ in $Li_{21}Si_5$, which represent all four symmetry-inequivalent Si sites in the structure. Not shown but equally true, a subset of these projected heavy atoms in Figure 14a also match the 14 Ir atoms closest to $(^1/_4, ^1/_4, ^1/_4)$ in $Mg_{44}Ir_7$, which represent all three symmetry-inequivalent Ir sites. The configuration of heavy atoms in $Sm_{11}Cd_{45}$, which is quite different from that of $Li_{21}Si_5$ and $Mg_{44}Ir_7$, appears in another region of the proposed quasicrystal. This region of projected heavy atoms (Figure 14b) matches closely with the 33 Sm atoms closest to $(^1/_4, ^1/_4, ^1/_4)$ in $Sm_{11}Cd_{45}$, which represent all five symmetry-inequivalent Sm sites. In still other regions of the proposed quasicrystal (of which Figure 14c is a representative example), the heavy atoms bear no obvious resemblance to the heavy atoms in $Li_{21}Si_5$, $Mg_{44}Ir_7$, or $Sm_{11}Cd_{45}$.

As Figure 14 shows, the quasicrystal can be thought of as containing domains which resemble all the quasicrystal approximants. At some locations, the heavy-atom structure resembles most that of $Sm_{11}Cd_{45}$, wheras in other places it is most like $Li_{21}Si_5$ and $Mg_{44}Ir_7$. Perhaps experimental quasicrystals will be found as intergrowths of two or more known quasicrystal approximant phases.

One more feature of this potential quasicrystal should be noted. In known quasicrystals, the quasicrystal belongs to a 3D point group that is inaccessible in 3D space groups (e.g. I_h). By contrast, for $t=\tau$, the resulting quasicrystal remains in 3D T_d symmetry. It is only in the improvement of its pseudo-symmetries that there is any additional symmetry in the cell-projected E_8 quasicrystal.

Conclusion

In the introduction to this paper, we catalogued all the metallic cubic structures which are not directly related to fcc, hcp, or bcc. In this paper, we have related roughly half of these structures to projections of the E_8 lattice. Of the remaining structures, some of them (e.g. Cr_3Si and YCd_6) are already known approximants related to 3D quasicrystals of I_h symmetry.[13,14] Taken together, it appears the majority of the common non-closest-packed cubic structures are connected to quasicrystal approximants.

The limitation to cubic structures may be an arbitrary one. It seems plausible that the E_8 lattice is related to tetrahedral packing in general, and not just to tetrahedral packing in cubic unit cells. Perhaps structures belonging to non-cubic Bravais classes will also prove to be so connected. We save such explorations for future work.

Acknowledgements

This research was supported by the National Science Foundation through grant DMR-0504703. We thank Aaron Bloomfield and Julie Fichot for their separate work in our laboratory on the $Li_{21}Si_5$ structure. We thank Roald Hoffmann for carefully listening to our ideas.

---

[1] P. Villars, L. Calvert, *Pearson's Handbook of Crystallographic Data for Intermetallic Phases*, 2nd ed., ASM International, Ohio (USA), **1991**.
[2] K. Lieser, H. Witte, *Z. Metallk.* **1952**, *43*, 396–401.
[3] Y. Chang, *Trans. Metall. Soc. AIME* **1968**, *242*, 1509–1515.
[4] J. Florio, R. Rundle, A. Snow, *Acta Crystallogr.* **1952**, *5*, 449–457.
[5] E. Zintl, W. Haucke, *Z. Elektrochem. Angew. Phys. Chem.* **1938**, *44*, 104–111.
[6] L. Misch, *Metallwirtsch., Metallwiss. Metalltech.* **1935**, *14*, 897–899.
[7] C. Gazzara, R. Middleton, R. Weiss, E. Hall, *Acta Crystallogr.* **1967**, *22*, 859–862.
[8] G. Yurko, J. Barton, J. Parr, *Acta Crystallogr.* **1959**, *12*, 909–911.
[9] C. Shoemaker, D. Shoemaker, T. Hopkins, S. Yindepit, *Acta Crystallogr.* **1978**, *B34*, 3573–3576.
[10] A. Bradley, P. Jones, *J. Inst. Met.* **1933**, *51*, 131–162.
[11] M. Fornasini, B. Chabot, E. Parthé, *Acta Crystallogr.* **1978**, *B34*, 2093–2099.
[12] A. Larson, D. Cromer, *Acta Crystallogr.* **1971**, *B27*, 1875–1879.
[13] Z. Wang, Q. Yang, K. Kuo, *Acta Crystallogr.* **1989**, *A45*, 268–274.
[14] H. Takakura, J. Guo, A. Tsai, *Philos. Mag. Lett.* **2001**, *81*, 411–418.
[15] V. Khare, N. Lalla, R. Tiwari, O. Srivastava, *J. Mater. Res.* **1995**, *10*, 1905–1912.
[16] J.-F. Sadoc, *J. Phys. Let.* **1983**, *44*, L707–L715.
[17] J.-F. Sadoc, R. Mosseri, *Geometrical Frustration*, Cambridge University Press, Cambridge (UK), **1999**.
[18] H. Coxeter, *Regular Polytopes*, 3rd ed., Dover Publications, New York (USA), **1973**.
[19] R. Berger, S. Lee, J. Johnson, B. Nebgen, F. Sha, J. Xu, *Chem. Eur. J.* **2008**, **2008**, *14*, 3908–3930.
[20] E. Jouffret, *Traité Elémentaire de Géométrie à Quatre Dimensions et Introduction à la Géométrie à n-Dimensions*, Gauthier-Villars, Paris (France), **1903**.
[21] H. Manning, *Geometry of Four Dimensions*, Macmillan, New York (USA), **1914**.
[22] M. Kléman, J.-F. Sadoc, *J. Phys. Let.* **1979**, *40*, L569–L574.
[23] D. Nelson, M. Widom, *Nucl. Phys.* **1984**, *B240*, 113–139.
[24] V. Elser, N. Sloane, *J. Phys. A* **1987**, *20*, 6161–6168.
[25] R. Moody, J. Patera, *J. Phys. A* **1993**, *26*, 2829–2853.
[26] J.-F. Sadoc, R Mosseri, *J. Phys. A* **1993**, *26*, 1789–1809.
[27] P. Kramer, R. Neri, *Acta Crystallogr.* **1984**, *A40*, 580–587.
[28] M. Duneau, A. Katz, *Phys. Rev. Lett.* **1985**, *54*, 2688–2691.
[29] P. Kalugin, A. Kitaev, L. Levitov, *Pis'ma Zh. Eksp. Teor. Fiz.* **1985**, *41*, 119–121.
[30] V. Elser, C. Henley, *Phys. Rev. Lett.* **1985**, *55*, 2883–2886.
[31] R. Nesper, H.-G. von Schnering, *J. Solid State Chem.* **1987**, *70*, 48–57.
[32] L. Westin, *Chem. Scr.* **1971**, *1*, 127–135.
[33] L. Westin, L.-E. Erdshammar, *Acta Chem. Scand.* **1972**, *26*, 3619–3626.
[34] R. Berger, S. Lee, R. Hoffmann, *Chem. Eur. J.* **2007**, *13*, 7852–7863.
[35] A. Johansson, S. Westman, *Acta Chem. Scand.* **1970**, *24*, 3471–3479.
[36] S. Samson, D. Hansen, *Acta Crystallogr.* **1972**, *B28*, 930–935.
[37] S. Samson, *Acta Crystallogr.* **1972**, *B28*, 936–945.
[38] L. Arnberg, A. Jonsson, S. Westman, *Acta Chem. Scand.* **1976**, *30*, 187–192.
[39] M. Booth, J. Brandon, R. Brizard, C. Chieh, W. Pearson, *Acta Crystallogr.* **1977**, *B33*, 30–36.
[40] A. Koster, J. Schoone, *Acta Crystallogr.* **1981**, *B37*, 1905–1907.
[41] S. Lidin, M. Jacob, A.-K. Larsson, *Acta Crystallogr.* **1994**, *C50*, 340–342.
[42] S. Mahne, B. Harbrecht, *J. Alloys Compd.* **1994**, *203*, 271–279.
[43] F. Bonhomme, K Yvon, *J. Alloys Compd.* **1995**, *227*, L1–L3.
[44] T. Nasch, W. Jeitschko, *J. Solid State Chem.* **1999**, *143*, 95–103.
[45] S. Thimmaiah, K. Richter, S. Lee, B. Harbrecht, *Solid State Sci.* **2003**, *5*, 1309–1317.
[46] W. Hornfeck, S. Thimmaiah, S. Lee, B. Harbrecht, *Chem. Eur. J.* **2004**, *10*, 4616–4626.

[47] V. Smetana, V. Babizhetskyy, G. Vajenine, A. Simon, *Angew. Chem.* **2006**, *118*, 6197–6200; *Angew. Chem. Int. Ed.* **2006**, *45*, 6051–6053.
[48] G. Friedel, *C. R. Acad. Sci. Paris* **1913**, *157*, 1533–1536.
[49] *Cerius2*, *v. 3.8*, Molecular Simulations: San Diego, CA, **1998**.
[50] M. Koca, R. Koç, M. Al-Barwani, *J. Phys. A* **2001**, *34*, 11210–11213.
[51] J. Conway, N. Sloane, *Sphere Packings, Lattices and Groups*, 3rd ed., Springer, New York (USA), **1999**.
[52] H. Nyman, S. Andersson, *Acta Crystallogr.* **1979**, *A35*, 580–583.
[53] H. Nyman, S. Andersson, *Acta Crystallogr.* **1979**, *A35*, 934–937.
[54] C. Janot, *Quasicrystals: A Primer*, 2nd ed., Clarendon, Oxford (UK), **1994**.
[55] B. Chabot, K. Cenzual, E. Parthé, *Acta Crystallogr.* **1981**, *A37*, 6–11.

Received: February 22, 2008